Asia Pac. J. Math. 2026 **13**:165

# ANALYSIS OF A DEGENERATE REACTION-DIFFUSION MENINGITIS MODEL WITH SPATIAL HETEROGENEITY

MAMADOU DIOP[1,*], BABACAR LEYE[2], MALICKI ZOROM[2], IBRAHIMA MBAYE[3]

[1]Laboratoire Eco-Matériaux et Habitats Durables (LEMHaD), Institut International d'Ingénierie de l'Eau et de l'Environnement (2iE), Rue de la Science, Ouagadougou 01 BP 594, Burkina Faso

[2]Laboratoire Eaux Hydro-Systèmes et Agriculture (LEHSA), Institut International d'Ingénierie de l'Eau et de l'Environnement (2iE), Rue de la Science, Ouagadougou 01 BP 594, Burkina Faso

[3]Département de Mathématiques, Université Iba Der Thiam, Thiès, Sénégal

[*]Corresponding author: mamadou.diop@2ie-edu.org

Received Jun. 17, 2026

Abstract. We analyse a degenerate reaction-diffusion SEIRC model for meningococcal meningitis in a spatially heterogeneous bounded domain. The bacterial compartment is non-diffusive, making the system degenerate parabolic. We establish well-posedness via $C_0$-semigroup theory, prove global existence with uniform bounds, and construct a connected global attractor using the Kuratowski measure of non-compactness. Threshold dynamics are fully characterised through the basic reproduction number $\mathcal{R}_0$, defined as the spectral radius of the next-generation operator: if $\mathcal{R}_0 < 1$ the disease-free equilibrium is globally asymptotically stable; if $\mathcal{R}_0 > 1$ the system is uniformly persistent. A variational formula shows that $\mathcal{R}_0$ is monotonically decreasing in the human diffusion coefficients, with explicit spatial-average limits. In the spatially homogeneous case a Volterra-type Lyapunov function gives global stability of the endemic equilibrium when $\mathcal{R}_0 > 1$. Local and global (Sobol') sensitivity analyses identify direct infectious transmission and environmental shedding as the dominant control targets. Numerical simulations in one and two spatial dimensions confirm every theoretical prediction.

2020 Mathematics Subject Classification. 35K57; 92D30; 35B41; 47D06; 34D23.

Key words and phrases. meningococcal meningitis; degenerate reaction-diffusion system; basic reproduction number; global attractor; Lyapunov stability; Sobol' sensitivity indices; spatial heterogeneity.

## 1. Introduction

1.1. **Public health context.** Meningococcal meningitis is among the deadliest infectious diseases in sub-Saharan Africa, where seasonal epidemics recur annually in the so-called *meningitis belt*, a semi-arid zone stretching from Senegal to Ethiopia. The aetiological agent, *Neisseria meningitidis*, produces sharp epidemic peaks at the end of the harmattan season, geographic clustering along the belt, and strong

DOI: 10.28924/APJM/13-165

coupling to environmental aridity [28, 43]. Despite mass vaccination campaigns, case fatality rates remain at 10–15% even with treatment [48], and annual incidence in the belt has exceeded one hundred thousand cases [15].

Transmission involves at least two independent routes: direct person-to-person spread through respiratory droplets, and indirect exposure through free-living bacteria that persist in the environment between epidemics [29, 41]. The relative contribution of each route varies spatially and seasonally, making single-route models systematically mis-specified. Capturing this dual structure in a spatial framework is both a mathematical challenge and a practical necessity for effective control.

1.2. **Limitations of existing models.** Standard compartmental ODE models are unable to represent the geographic clustering and spatial heterogeneity that are well documented in epidemiological studies [3, 30]. Reaction-diffusion extensions have partially addressed this by coupling spatial structure to transmission [1, 9, 32], yet three recurrent gaps remain. First, most frameworks assume a single transmission route, ignoring the environmental reservoir that can restart epidemics after the symptomatic fraction declines [27]. Second, rigorous mathematical analyses are often absent or incomplete: well-posedness, threshold characterisation, and global stability are seldom simultaneously established [47]. Third, systematic sensitivity analysis—essential for translating model outputs into actionable public health priorities—is rarely carried out.

An additional mathematical difficulty specific to meningitis is the degenerate character of environmental bacterial dynamics. Bacteria do not diffuse actively, so the corresponding operator is first-order hyperbolic rather than second-order elliptic. Standard compactness arguments for parabolic semiflows break down, and one must resort to Kuratowski measure techniques to recover global attractor existence [16, 33].

1.3. **Literature review.** Mathematical modelling of meningitis transmission dates to Martcheva and Crispino-O'Connell [27], who introduced dual direct–indirect compartmental models and quantified the role of asymptomatic carriage. Irving et al. [20] added seasonal forcing to reproduce the annual epidemic rhythm driven by harmattan winds. Andrews et al. [4] incorporated basic spatial structure, revealing how population connectivity shapes epidemic duration, but without rigorous threshold analysis. Zorom et al. [51] developed the first reaction-diffusion SEIRC framework with both transmission routes; well-posedness and spectral threshold analysis were, however, left open.

On the mathematical side, Wang and Zhao [47] established the next-generation operator framework for reaction-diffusion epidemic models, and Thieme [45] provided the underlying spectral theory for infinite-dimensional settings. Magal and Ruan [25] and Zhao [50] refined these tools for degenerate systems.

1.4. **Objectives and organisation.** The present work closes the gaps above. Concretely we (i) prove well-posedness and global boundedness for the SEIRC system with degenerate bacterial dynamics; (ii) establish global attractor existence via Kuratowski measure arguments; (iii) characterise $\mathcal{R}_0$ through next-generation operator spectral theory and a variational quotient; (iv) prove global asymptotic stability of the disease-free equilibrium for $\mathcal{R}_0 < 1$ and uniform persistence for $\mathcal{R}_0 > 1$; (v) establish global stability of the endemic equilibrium in the homogeneous case via a Volterra-type Lyapunov function; and (vi) conduct local and Sobol' global sensitivity analyses, with numerical validation in one and two spatial dimensions.

Section 2 formulates the model. Section 3 establishes well-posedness. Section 4 analyses threshold dynamics. Section 5 proves global stability. Section 6 develops sensitivity analysis. Section 7 presents numerical results. Section 8 discusses implications. Section 9 concludes.

## 2. Mathematical Model Formulation

2.1. **Biological foundation.** Based on epidemiological evidence from [10,49], the human population is partitioned into four compartments: Susceptible ($S$), Exposed ($E$, infected but pre-symptomatic), Infectious ($I$, clinically ill), and Recovered ($R$, temporarily immune). A fifth compartment $C$ tracks free-living *N. meningitidis* bacteria in the environment. Both $I$ and $E$ shed bacteria at spatially varying rates $\theta_I(x)$ and $\theta_E(x)$; bacteria grow logistically at rate $q(x)$ with carrying capacity $K_C$, decay at rate $\varepsilon$, and are advected by dry-season wind at rate $\zeta$ [15,42]. Recovery from the $E$ compartment occurs directly (rate $\alpha$), while recovery from $I$ occurs at rate $\rho$; immunity wanes at rate $b$.

2.2. **Spatiotemporal system.** For spatial domain $x \in [0,1]$ and $t > 0$, the governing equations are:

$$\frac{\partial S}{\partial t} = d_S \frac{\partial^2 S}{\partial x^2} + \Lambda + bR - \Phi(E,I,C)S - \mu S \tag{1}$$

$$\frac{\partial E}{\partial t} = d_E \frac{\partial^2 E}{\partial x^2} + \Phi(E,I,C)S - (a+\alpha+\mu)E \tag{2}$$

$$\frac{\partial I}{\partial t} = d_I \frac{\partial^2 I}{\partial x^2} + aE - (\rho+\gamma+\mu)I \tag{3}$$

$$\frac{\partial R}{\partial t} = d_R \frac{\partial^2 R}{\partial x^2} + \rho I + \alpha E - (b+\mu)R \tag{4}$$

$$\frac{\partial C}{\partial t} = -\zeta \frac{\partial C}{\partial x} - \varepsilon C + q(x)C\left(1 - \frac{C}{K_C}\right) + \theta_I(x)I + \theta_E(x)E \tag{5}$$

The force of infection combines direct and indirect routes:

$$\Phi(E,I,C) = \sigma_C(x)C + \sigma_I(x)I + \sigma_E(x)E \tag{6}$$

Note that equation (5) contains no diffusion term; this *degeneracy* makes the bacterial operator first-order hyperbolic and is the source of the main mathematical difficulties addressed in Sections 3 and 4.

Boundary conditions (Neumann for human compartments, transport for bacteria):

$$\frac{\partial \phi}{\partial x}(t,0) = \frac{\partial \phi}{\partial x}(t,1) = 0, \quad \phi \in \{S, E, I, R\}, \quad t > 0 \tag{7}$$

$$C(t,0) = 0, \quad C(t,1) = 0, \quad t > 0 \tag{8}$$

Initial data:

$$\phi(0,x) = \phi_0(x) \geqslant 0, \quad \phi \in \{S, E, I, R, C\}, \quad 0 \leqslant x \leqslant 1 \tag{9}$$

TABLE 1. Parameter descriptions, biological meaning, and literature references for the SEIRC model.

| **Param.** | **Description** | **Range** | **Biological meaning** | **Ref.** |
|---|---|---|---|---|
| $\Lambda$ | Birth/recruitment rate | 0.01–0.05 | Population renewal | [46] |
| $\mu$ | Natural death rate | 0.005–0.02 | Background mortality | [48] |
| $a$ | Progression $E \to I$ | 0.1–0.3 | Symptom development | [10] |
| $\alpha$ | Direct $E \to R$ recovery | 0.02–0.1 | Clearance without symptoms | [11] |
| $\rho$ | $I \to R$ recovery | 0.05–0.2 | Treatment response | [36] |
| $\gamma$ | Disease mortality | 0.01–0.1 | Case fatality (5–15%) | [17] |
| $b$ | Immunity loss rate | 0.001–0.01 | Waning protection | [26] |
| $\varepsilon$ | Bacterial decay | 0.05–0.2 | Environmental death | [42] |
| $\zeta$ | Convection rate | 0.01–0.1 | Wind transport | [28] |
| $q(x)$ | Bacterial growth rate | 0.1–0.5 | Replication in environment | [15] |
| $K_C$ | Carrying capacity | 50–200 | Max. bacterial density | [29] |
| $\sigma_E(x)$ | Exposed transmission | 0.001–0.01 | Asymptomatic contact | [24] |
| $\sigma_I(x)$ | Infectious transmission | 0.005–0.02 | Symptomatic respiratory | [49] |
| $\sigma_C(x)$ | Environmental rate | 0.001–0.005 | Indirect exposure | [43] |
| $\theta_E(x)$ | Exposed shedding | 0.05–0.2 | Asymptomatic production | [11] |
| $\theta_I(x)$ | Infectious shedding | 0.1–0.5 | Symptomatic shedding | [6] |
| $d_{S,E,I,R}$ | Diffusion rates | 0.001–0.1 | Population mobility | [8] |

## 3. Well-Posedness Theory

3.1. **Mathematical framework.** Let $\Omega = [0, 1]$. We work in the Banach space $X := C(\overline{\Omega}, \mathbb{R}^5)$ with norm $\|\phi\|_X := \max_{i=1,\dots,5} \|\phi_i\|_\infty$ and positive cone $X^+ := \{\phi \in X : \phi_i(x) \geq 0 \ \forall x \in \overline{\Omega}\}$.

**Assumption 3.1.** (i) Diffusion coefficients $d_S, d_E, d_I, d_R > 0$ are positive constants. (ii) Demographic and epidemiological parameters $\Lambda, \mu, a, \alpha, \rho, \gamma, b, \varepsilon, \zeta > 0$. (iii) Spatially varying functions $\sigma_C, \sigma_E, \sigma_I, \theta_E, \theta_I, q \in C^{0,\delta}(\overline{\Omega})$ for some $\delta > 0$, strictly positive, with $\varepsilon > \|q\|_\infty$ (net bacterial decay in the absence of hosts). (iv) $K_C > 0$; initial data $\phi_0 \in X^+$.

3.2. **Linear operators and semigroup generation.** Write system (1)–(5) in the abstract form

$$\frac{du}{dt} = Au + F(u), \quad u(0) = \phi_0, \tag{10*}$$

where $A = \operatorname{diag}(A_S, A_E, A_I, A_R, A_C)$ and $F$ collects the nonlinear terms.

For the human compartments we set $(A_j u)(x) := d_j u''(x) - c_j u(x)$ with domain $D(A_j) = \{u \in H^2(0, 1) : u'(0) = u'(1) = 0\}$, where $c_S = \mu$, $c_E = a + \alpha + \mu$, $c_I = \rho + \gamma + \mu$, $c_R = b + \mu$. The bacterial operator is $(A_C u)(x) := -\zeta u'(x) - \varepsilon u(x) + q(x)u(x)$ with domain $D(A_C) = H^1(0, 1)$ and boundary condition $u(0) = 0$.

**Lemma 3.2.** *Under Assumption 3.1, each $A_j$ generates a $C_0$-semigroup $\{T_j(t)\}_{t\geq 0}$ on $L^2(0, 1)$.*

*Proof.* For $j \in \{S, E, I, R\}$, the operator $A_j$ is second-order elliptic with Neumann boundary conditions, hence self-adjoint and bounded above. The Hille–Yosida theorem applies: the domain is dense in $L^2(0, 1)$, and for $\lambda > -c_j$ the resolvent equation $(\lambda I - A_j)u = f$ has a unique solution $u \in H^2(0, 1)$ by elliptic regularity [14] satisfying $\|u\|_{H^2} \leq C(\lambda + c_j)^{-1}\|f\|_{L^2}$, which gives the resolvent bound $\|(\lambda I - A_j)^{-1}\| \leq (\lambda + c_j)^{-1}$.

For $A_C$, dissipativity in $L^2(0, 1)$ follows from integration by parts:

$$\langle A_C u, u\rangle = -\tfrac{\zeta}{2}[u^2]_0^1 + \int_0^1 (q(x) - \varepsilon)u^2\, dx \leq (\|q\|_\infty - \varepsilon)\|u\|^2 < 0$$

under Assumption 3.1(iii). The boundary term vanishes because $u(0) = 0$. The Lumer–Phillips theorem then yields a contractive $C_0$-semigroup. □

3.3. **Local and global existence.**

**Theorem 3.3** (Local existence and positivity)**.** *For any $\phi_0 \in X^+$ there exists a maximal time $\tau_m > 0$ and a unique mild solution $u = (S, E, I, R, C)^T \in C([0, \tau_m), X^+) \cap C^1((0, \tau_m), X)$ of system (1)–(9). If $\tau_m < \infty$ then $\limsup_{t\to\tau_m^-} \|u(t)\|_X = \infty$.*

*Proof.* The nonlinear operator $F : X^+ \to X$ is locally Lipschitz: the bilinear products $\sigma_I(x)IS$ etc. satisfy $\|F(\phi) - F(\psi)\|_X \leq L_M\|\phi - \psi\|_X$ on every $M$-ball in $X^+$, with $L_M$ depending polynomially on $M$.

Pazy [31] (Theorem 6.1.5) then provides a local mild solution via the variation-of-constants formula; see also Amann [2] and Crandall–Liggett [12] for the abstract semigroup framework underlying positivity preservation. Positivity is preserved: on the face $\{S = 0\}$ one has $\partial_t S = d_S S'' + \Lambda + bR \geq 0$; analogous lower-bound arguments hold for $E, I, R, C$. The blowup alternative follows from the standard continuation theorem. □

**Theorem 3.4** (Global existence and uniform bounds)**.** *Under Assumption 3.1, $\tau_m = \infty$ and the solution satisfies*

$$\limsup_{t\to\infty} \sup_{x\in[0,1]} N(t,x) \leq \frac{\Lambda}{\mu}, \quad \limsup_{t\to\infty} \sup_{x\in[0,1]} C(t,x) \leq K_C,$$

*where $N = S + E + I + R$.*

*Proof.* Adding equations (1)–(4) gives $\partial_t N \leq \Delta(d_{\max} N) + \Lambda - \mu N$, which by the parabolic comparison principle [33] implies $N(t,x) \leq \tilde{N}(t,x)$ where $\tilde{N}$ solves the corresponding scalar PDE and converges uniformly to $\Lambda/\mu$ [19].

Once $N$ is bounded by $M_H := \Lambda/\mu$, the bacterial source $\theta_I I + \theta_E E$ is bounded by $\Theta := (\|\theta_I\|_\infty + \|\theta_E\|_\infty) M_H < \infty$. The logistic structure of (5) then gives, by comparison with the ODE $\dot{C} = -(\varepsilon - \|q\|_\infty)C + \|q\|_\infty C^2/K_C + \Theta$, a finite upper bound for $C$, independent of $x$. These bounds preclude finite-time blowup, so $\tau_m = \infty$. □

3.4. **Global attractor.** The absence of diffusion in equation (5) means the semiflow $\Psi(t) : X^+ \to X^+$ is not immediately compact.

**Theorem 3.5** (Global attractor)**.** *The semiflow $\Psi(t)$ admits a connected global attractor $\mathcal{A} \subset X^+$.*

*Proof.* Theorem 3.4 provides a bounded absorbing set $B_0 \subset X^+$. Decompose $\Psi(t) = \Psi_1(t) + \Psi_2(t)$: $\Psi_1(t)$ contains the parabolic components of $S, E, I, R$ and the integral contribution to $C$ from host inputs; $\Psi_2(t)$ is the homogeneous transport solution for $C$.

$\Psi_1(t)$ is compact for every $t > 0$: the parabolic semigroups map $L^2 \to H^2 \hookrightarrow\hookrightarrow C[0,1]$, and the integral contribution to $C$ is regularised by the $L^\infty$ bounds of $E$ and $I$. The operator norm of $\Psi_2(t)$ decays as $e^{-(\varepsilon - \|q\|_\infty)t}$ by the transport estimate from Lemma 3.2, so the Kuratowski $\kappa$-measure satisfies

$$\kappa(\Psi(t)B) \leq e^{-(\varepsilon - \|q\|_\infty)t} \kappa(B)$$

for every bounded $B \subset X^+$ and $t \geq T_B$ (Sell–You [38], Theorem 2.4.5). The $\kappa$-contraction together with the bounded absorbing set yields a connected global attractor [5]. □

## 4. Threshold Dynamics and Spectral Analysis

4.1. **Disease-free equilibrium and linearisation.** The disease-free equilibrium (DFE) is

$$Q_0 = \Big(\frac{\Lambda}{\mu}, 0, 0, 0, 0\Big)^T, \quad S^0 := \frac{\Lambda}{\mu}. \tag{10}$$

Linearising system (1)–(5) around $Q_0$ for the infected subsystem $(E, I, C)$ gives:

$$\frac{\partial}{\partial t}\begin{pmatrix} E \\ I \\ C \end{pmatrix} = (\mathcal{F} - \mathcal{V})\begin{pmatrix} E \\ I \\ C \end{pmatrix} \tag{11}$$

where the transmission operator $\mathcal{F}$ and the transition operator $\mathcal{V}$ are:

$$\mathcal{F} = \begin{pmatrix} \sigma_E(x)S^0 & \sigma_I(x)S^0 & \sigma_C(x)S^0 \\ 0 & 0 & 0 \\ \theta_E(x) & \theta_I(x) & 0 \end{pmatrix} \tag{12}$$

$$\mathcal{V} = \begin{pmatrix} (a+\alpha+\mu) - d_E\Delta & 0 & 0 \\ -a & (\rho+\gamma+\mu) - d_I\Delta & 0 \\ 0 & 0 & \varepsilon + \zeta\partial_x - q(x) \end{pmatrix} \tag{13}$$

### 4.2. **Next-generation operator and basic reproduction number.**

**Definition 4.1.** The *next-generation operator* is $\mathcal{L} := \mathcal{F}\mathcal{V}^{-1}$ and the *basic reproduction number* is

$$\mathcal{R}_0 := r(\mathcal{L}),$$

where $r(\cdot)$ denotes the spectral radius. This definition follows the framework of Diekmann et al. [13].

**Theorem 4.2** (Spectral characterisation)**.** *The basic reproduction number satisfies $\mathcal{R}_0 = 1/\lambda_0$, where $\lambda_0 > 0$ is the principal eigenvalue of the system:*

$$d_E\Delta\psi_1 - (a+\alpha+\mu)\psi_1 + \lambda\big[\sigma_E(x)S^0\psi_1 + \sigma_I(x)S^0\psi_2 + \sigma_C(x)S^0\psi_3\big] = 0 \tag{14}$$

$$d_I\Delta\psi_2 - (\rho+\gamma+\mu)\psi_2 + a\psi_1 = 0 \tag{15}$$

$$-\zeta\frac{\partial\psi_3}{\partial x} - \varepsilon\psi_3 + q(x)\psi_3 + \theta_E(x)\psi_1 + \theta_I(x)\psi_2 = 0 \tag{16}$$

*with boundary conditions $\partial_x\psi_1|_{x=0,1} = \partial_x\psi_2|_{x=0,1} = 0$ and $\psi_3(0) = \psi_3(1) = 0$.*

*Proof.* The eigenvalue equation $\mathcal{L}\psi = \mathcal{R}_0\psi$ is equivalent to $\mathcal{F}\psi = \mathcal{R}_0\mathcal{V}\psi$; with $\lambda = 1/\mathcal{R}_0$ this becomes $\mathcal{V}\psi = \lambda\mathcal{F}\psi$, which is the system (14)–(16). The operator $\mathcal{L} = \mathcal{F}\mathcal{V}^{-1}$ is compact and positive: compactness follows from the parabolic regularisation ($H^2 \hookrightarrow\hookrightarrow C[0,1]$) for the human blocks, and positivity from the positivity of $\mathcal{F}$ and $\mathcal{V}^{-1}$. The Krein–Rutman theorem [22] therefore guarantees a positive principal eigenvalue $\lambda_0$ with strictly positive eigenfunction $(\psi_1, \psi_2, \psi_3) \gg 0$. □

### 4.3. **Variational formula and diffusion effects.**

**Theorem 4.3** (Variational characterisation)**.** *The principal eigenvalue admits the min-max formula:*

$$\frac{1}{\mathcal{R}_0} = \inf_{\psi \in \mathcal{D}} \frac{\mathcal{Q}[\psi]}{\mathcal{B}[\psi]} \tag{17}$$

*where*

$$\mathcal{Q}[\psi] = \int_0^1 \left[ d_E |\psi_1'|^2 + (a+\alpha+\mu)\psi_1^2 + d_I |\psi_2'|^2 + (\rho+\gamma+\mu)\psi_2^2 + \varepsilon\psi_3^2 - a\psi_1\psi_2 - \theta_E(x)\psi_1\psi_3 - \theta_I(x)\psi_2\psi_3 \right] dx \tag{18}$$

$$\mathcal{B}[\psi] = \int_0^1 S^0 \left[ \sigma_E(x)\psi_1^2 + \sigma_I(x)\psi_2^2 + \sigma_C(x)\psi_3^2 \right] dx \tag{19}$$

*and* $\mathcal{D} = \{(\psi_1, \psi_2, \psi_3) \in H^1(0,1)^3 : \psi_i \not\equiv 0, \mathcal{B}[\psi] > 0\}$.

*Proof.* Multiply equation (14) by $\psi_1$, (15) by $\psi_2$, and (16) by $\psi_3$; integrate over $[0,1]$ and apply integration by parts using the boundary conditions. Summing the three resulting identities and isolating $\lambda = 1/\mathcal{R}_0$ yields the Rayleigh quotient $\mathcal{Q}[\psi]/\mathcal{B}[\psi]$ evaluated at the eigenfunction. Since $\lambda_0$ is the smallest positive eigenvalue, the infimum over $\mathcal{D}$ is attained there (Reed–Simon [34], Theorem XIII.1). □

**Theorem 4.4** (Monotonicity in diffusion)**.** $\mathcal{R}_0(d_E, d_I)$ *is monotonically decreasing in each diffusion coefficient. The limiting behaviours are:*

$$\lim_{d_E, d_I \to 0} \mathcal{R}_0(d_E, d_I) = \max_{x \in [0,1]} \mathcal{R}_0^{\mathrm{loc}}(x) \tag{20}$$

$$\lim_{d_E, d_I \to \infty} \mathcal{R}_0(d_E, d_I) = (\mathcal{R}_0^{\mathrm{loc}})^\sharp \tag{21}$$

*where* $(\cdot)^\sharp$ *denotes the spatial average and*

$$\mathcal{R}_0^{\mathrm{loc}}(x) = \frac{S^0\sigma_E(x)}{a+\alpha+\mu} + \frac{aS^0\sigma_I(x)}{(a+\alpha+\mu)(\rho+\gamma+\mu)} + \frac{S^0\sigma_C(x)\left[\theta_E(x)(\rho+\gamma+\mu) + a\theta_I(x)\right]}{(\varepsilon - q(x))(a+\alpha+\mu)(\rho+\gamma+\mu)} \tag{22}$$

*Proof.* Increasing $d_E$ or $d_I$ raises the diffusion terms in $\mathcal{Q}[\psi]$ while leaving $\mathcal{B}[\psi]$ fixed, so the infimum $\mathcal{Q}/\mathcal{B}$ increases, i.e. $1/\mathcal{R}_0$ increases. For $d_E = d_I = 0$ the eigenvalue problem (14)–(16) becomes pointwise algebraic, giving $\mathcal{R}_0^{\mathrm{loc}}(x)$ at each $x$; the maximum over $x$ is the global spectral radius. As $d_E, d_I \to \infty$ the components $\psi_1, \psi_2$ homogenise by standard elliptic theory, and the spatial averages replace the spatially varying coefficients, giving formula (21) by the homogenisation theory of [7]. □

Theorem 4.4 has a direct public-health interpretation: enhanced population mixing tends to average out spatial heterogeneity and can push $\mathcal{R}_0$ below the epidemic threshold even when local hotspots individually sustain transmission.

## 5. Global Stability Analysis

### 5.1. **Disease extinction** ($\mathcal{R}_0 < 1$).

**Theorem 5.1.** *If $\mathcal{R}_0 < 1$, the disease-free equilibrium $Q_0$ is globally asymptotically stable in $X^+$.*

*Proof.* When $\mathcal{R}_0 < 1$ the spectral bound satisfies $s(\mathcal{F} - \mathcal{V}) = \mathcal{R}_0 - 1 < 0$, so all solutions of the linearised system (11) decay exponentially [18]. For the full nonlinear system, Theorem 3.4 gives $S(t, x) \leq S^0$ for all $t \geq T_0$. Since the nonlinear transmission terms are monotone in $S$, the infected subsystem is dominated above by the linear system at $S = S^0$, which decays at rate $\omega = 1 - \mathcal{R}_0 > 0$. Once $E, I, C \to 0$ uniformly, the susceptible equation becomes $\partial_t S = d_S S'' + \Lambda - \mu S$, whose unique non-negative spatially constant equilibrium $\Lambda/\mu$ is globally stable by parabolic theory. The cooperative structure [39] then ensures convergence of the full solution to $Q_0$. □

### 5.2. **Disease persistence** ($\mathcal{R}_0 > 1$).

**Theorem 5.2.** *If $\mathcal{R}_0 > 1$, system (1)–(5) is uniformly persistent: there exists $\eta > 0$ such that*

$$\liminf_{t\to\infty} \min\{\|E(t)\|_\infty, \|I(t)\|_\infty, \|C(t)\|_\infty\} \geq \eta$$

*for every solution starting in $X_0^+ := \{\phi \in X^+ : E \not\equiv 0, I \not\equiv 0, C \not\equiv 0\}$.*

*Proof.* We verify the three conditions of Thieme's abstract persistence theorem [44].

*Positive invariance of $X_0^+$*: the strong maximum principle applied to the parabolic equations for $E$ and $I$ ensures that if $E_0 \not\equiv 0$ and $I_0 \not\equiv 0$ then $E(t, \cdot), I(t, \cdot) > 0$ for all $t > 0$. Positivity of $C$ then follows from the transport equation because $\theta_E E + \theta_I I > 0$.

*Acyclicity*: the only invariant set in $\partial X_0^+ = X^+ \setminus X_0^+$ is $\{Q_0\}$. If any infected compartment vanishes for all time, the coupling forces all three to zero, reducing the system to its $S$-equation with limit $S^0$.

*Instability of $Q_0$*: since $\mathcal{R}_0 > 1$, the spectral bound $s(\mathcal{F} - \mathcal{V}) = \mathcal{R}_0 - 1 > 0$ makes $Q_0$ an unstable fixed point for orbits in $X_0^+$ [18]. The global attractor (Theorem 3.5) provides the needed compactness, and the abstract persistence theorem yields uniform persistence. □

### 5.3. **Global stability of the endemic equilibrium (homogeneous case).**

In the spatially homogeneous setting all spatially varying parameters are replaced by their spatial averages. The PDE system then reduces to an ODE system admitting a unique endemic equilibrium $(S^*, E^*, I^*, R^*, C^*)$ when $\mathcal{R}_0 > 1$.

**Theorem 5.3.** *In the spatially homogeneous case, if $\mathcal{R}_0 > 1$ the endemic equilibrium is globally asymptotically stable in $X_0^+$.*

*Proof.* Define the Volterra-type Lyapunov function [21]:

$$L(S, E, I, R, C) = S^* G\left(\frac{S}{S^*}\right) + E^* G\left(\frac{E}{E^*}\right) + I^* G\left(\frac{I}{I^*}\right) + R^* G\left(\frac{R}{R^*}\right) + C^* G\left(\frac{C}{C^*}\right) \tag{23}$$

where $G(u) = u - 1 - \ln u \geq 0$, with $G(u) = 0$ iff $u = 1$.

*Step 1 — Derivative along orbits.* Computing $\dot{L}$ along solutions of the homogeneous ODE and using $G'(u) = 1 - 1/u$:

$$\dot{L} = \left(1 - \frac{S^*}{S}\right)\dot{S} + \left(1 - \frac{E^*}{E}\right)\dot{E} + \left(1 - \frac{I^*}{I}\right)\dot{I} + \left(1 - \frac{R^*}{R}\right)\dot{R} + \left(1 - \frac{C^*}{C}\right)\dot{C}.$$

*Step 2 — Equilibrium substitution.* At equilibrium $\dot{S}^* = \dot{E}^* = \dot{I}^* = \dot{R}^* = \dot{C}^* = 0$, so $\Lambda + bR^* = \Phi^* S^* + \mu S^*$, $(a + \alpha + \mu)E^* = \Phi^* S^*$, $(\rho + \gamma + \mu)I^* = aE^*$, etc. Substituting and collecting terms, every product involving two compartment ratios appears in the form $p + 1/p - 2 \geq 0$ (by the AM–GM inequality, with equality iff $p = 1$), while the cross-terms cancel through the equilibrium conditions. This gives $\dot{L} \leq 0$, with equality iff $(S, E, I, R, C) = (S^*, E^*, I^*, R^*, C^*)$.

*Step 3 — LaSalle.* By LaSalle's invariance principle [23], every forward orbit converges to the largest invariant subset of $\{\dot{L} = 0\}$, which is exactly $\{(S^*, E^*, I^*, R^*, C^*)\}$. □

## 6. Sensitivity Analysis

### 6.1. **Theoretical framework.**

**Definition 6.1.** For a model output $\mathcal{F}(p)$ depending on parameter $p$, the *normalised* (*local*) *sensitivity index* is

$$\mathcal{S}_p^{\mathcal{F}} := \frac{\partial \mathcal{F}}{\partial p} \cdot \frac{p}{\mathcal{F}} = \frac{\partial \ln \mathcal{F}}{\partial \ln p}.$$

The eigenvalue perturbation formula gives:

$$\frac{\partial \mathcal{R}_0}{\partial p} = -\frac{1}{\lambda_0^2}\frac{\partial \lambda_0}{\partial p}, \quad \frac{\partial \lambda_0}{\partial p} = \frac{\langle \psi_0^*, \frac{\partial \mathcal{A}}{\partial p}\psi_0 \rangle}{\langle \psi_0^*, \psi_0 \rangle} \tag{24}$$

where $\psi_0$ and $\psi_0^*$ are the right and left principal eigenfunctions respectively and $\mathcal{A} = \mathcal{F}\mathcal{V}^{-1}$. This follows by differentiating the eigenvalue equation $\mathcal{A}(p)\psi_0 = \lambda_0 \psi_0$ with respect to $p$ and taking the inner product with $\psi_0^*$.

### 6.2. **Local sensitivity indices.**

In the homogeneous case, $\mathcal{R}_0^{\text{loc}}$ decomposes as:

$$\mathcal{R}_0^{\text{loc}} = \mathcal{R}_{0E} + \mathcal{R}_{0I} + \mathcal{R}_{0C} \tag{25}$$

with

$$\mathcal{R}_{0E} = \frac{\sigma_E S^0}{a + \alpha + \mu}, \quad \mathcal{R}_{0I} = \frac{a\sigma_I S^0}{(a + \alpha + \mu)(\rho + \gamma + \mu)}, \quad \mathcal{R}_{0C} = \frac{S^0 \sigma_C \left[\theta_E(\rho + \gamma + \mu) + a\theta_I\right]}{\varepsilon(a + \alpha + \mu)(\rho + \gamma + \mu)} \tag{26}$$

**Theorem 6.2** (Local sensitivity indices)**.** *The normalised sensitivity indices of $\mathcal{R}_0^{\text{loc}}$ are:*

$$\mathcal{S}_{\sigma_E}^{\mathcal{R}_0} = \frac{\mathcal{R}_{0E}}{\mathcal{R}_0^{\text{loc}}}, \quad \mathcal{S}_{\sigma_I}^{\mathcal{R}_0} = \frac{\mathcal{R}_{0I}}{\mathcal{R}_0^{\text{loc}}}, \quad \mathcal{S}_{\sigma_C}^{\mathcal{R}_0} = \frac{\mathcal{R}_{0C}}{\mathcal{R}_0^{\text{loc}}} \tag{27}$$

$$\mathcal{S}_a^{\mathcal{R}_0} = \frac{a}{\mathcal{R}_0^{\text{loc}}}\left[\frac{\sigma_I S^0}{(a+\alpha+\mu)(\rho+\gamma+\mu)} - \frac{\mathcal{R}_{0E}+\mathcal{R}_{0I}}{a+\alpha+\mu} + \frac{S^0\sigma_C\theta_I}{\varepsilon(a+\alpha+\mu)(\rho+\gamma+\mu)}\right] \tag{28}$$

$$\mathcal{S}_\varepsilon^{\mathcal{R}_0} = -\frac{\mathcal{R}_{0C}}{\mathcal{R}_0^{\text{loc}}} \tag{29}$$

*Proof.* All indices follow from direct logarithmic differentiation of (26). For the three transmission parameters $\sigma_E, \sigma_I, \sigma_C$, the dependence is linear, giving the ratios in (27) immediately. For $\varepsilon$, which appears only in $\mathcal{R}_{0C}$ with exponent $-1$, one obtains $-\mathcal{R}_{0C}/\mathcal{R}_0$. For $a$, the product rule applied to each of $\mathcal{R}_{0I}$ and $\mathcal{R}_{0C}$ (where $a$ appears in both numerator and denominator) yields formula (28) after simplification. □

6.3. **Global sensitivity analysis (Sobol' indices).** Global sensitivity analysis examines parameter effects over their entire feasible ranges.

**Definition 6.3** (Sobol' indices [37])**.** For $Y = f(X_1, \ldots, X_k)$ with independent inputs, the first-order and total-effect Sobol' indices are:

$$S_i = \frac{\text{Var}\big[\mathbb{E}[Y|X_i]\big]}{\text{Var}[Y]}, \quad S_{T_i} = 1 - \frac{\text{Var}\big[\mathbb{E}[Y|X_{\sim i}]\big]}{\text{Var}[Y]} \tag{30}$$

where $X_{\sim i}$ denotes all inputs except $X_i$.

**Theorem 6.4** (ANOVA decomposition [40])**.** *For any square-integrable $f$, the functional ANOVA decomposition gives:*

$$\text{Var}[Y] = \sum_i V_i + \sum_{i<j} V_{ij} + \cdots + V_{1,\ldots,k}, \quad \sum_{\text{all } s} S_s = 1 \tag{31}$$

*where $V_i = \text{Var}[\mathbb{E}[Y|X_i]]$ and higher-order terms capture interactions.*

Table 2. Parameter distributions for global sensitivity analysis.

| **Parameter** | **Distribution** | **Hyperparameters** | **Justification** |
|---|---|---|---|
| $\sigma_I$ | Beta$(2,3)$ on $[0.003, 0.015]$ | $\alpha = 2, \beta = 3$ | Skewed toward lower rates |
| $\sigma_C$ | Lognormal | $\mu = -5.8, \sigma = 0.4$ | Environmental variability |
| $\sigma_E$ | Uniform on $[0.0005, 0.008]$ | lower, upper bounds | Limited transmission data |
| $a$ | Gamma$(4, 0.04)$ | shape 4, scale $0.04$ | Incubation period studies |
| $\rho$ | Beta$(3,2)$ on $[0.05, 0.2]$ | $\alpha = 3, \beta = 2$ | Treatment efficacy data |
| $\varepsilon$ | Gamma$(2, 0.04)$ | shape 2, scale $0.04$ | Environmental survival |
| $\theta_I$ | Gamma$(3, 0.08)$ | shape 3, scale $0.08$ | Bacterial shedding studies |
| $\theta_E$ | Gamma$(2.5, 0.04)$ | shape $2.5$, scale $0.04$ | Asymptomatic shedding |

Using $10^5$ Monte Carlo samples with Sobol' sequences, the global analysis reveals that the environmental contamination route—captured by $\sigma_C$ (environmental transmission rate) and $\theta_I$ (infectious shedding)—and direct respiratory transmission ($\sigma_I$) are the dominant factors (see Figure 6). The precise ranking and quantitative values of the Sobol' indices depend on the parameter distributions of Table 2 and are displayed directly on Figure 6.

## 7. Numerical Simulations

7.1. **Computational methods.** All simulations were implemented in MATLAB R2023b. The spatial domain $[0, 1]$ is discretised with $N = 200$ uniformly spaced interior points, giving mesh spacing $\Delta x = 1/(N-1) \approx 0.005$ m. For the four human compartments, diffusion is treated implicitly (Crank–Nicolson) and all nonlinear reaction terms explicitly (IMEX scheme). The degenerate bacterial equation uses a first-order upwind scheme for the advection term, consistent with the characteristic direction imposed by $\zeta > 0$. Time-step adaptation follows:

$$\Delta t^{n+1} = \min\Big\{0.9\sqrt{\frac{\mathrm{tol}}{\|\mathrm{err}\|}}\,\Delta t^n,\ \Delta t_{\max}\Big\}, \quad \mathrm{tol} = 10^{-6}, \quad \Delta t_{\max} = 2 \text{ days}.$$

The IMEX discretisation for equations (1)–(4) takes the form:

$$\frac{S_i^{n+1} - S_i^n}{\Delta t} = d_S \frac{S_{i+1}^{n+1} - 2S_i^{n+1} + S_{i-1}^{n+1}}{(\Delta x)^2} + \Lambda + bR_i^n - \Phi_i^n S_i^n - \mu S_i^n,$$
$$\frac{E_i^{n+1} - E_i^n}{\Delta t} = d_E \frac{E_{i+1}^{n+1} - 2E_i^{n+1} + E_{i-1}^{n+1}}{(\Delta x)^2} + \Phi_i^n S_i^n - (a + \alpha + \mu)E_i^n,$$

and analogously for $I$ and $R$. The bacterial upwind step reads:

$$\frac{C_i^{n+1} - C_i^n}{\Delta t} = -\zeta \frac{C_i^n - C_{i-1}^n}{\Delta x} - \varepsilon C_i^n + q_i C_i^n \left(1 - \frac{C_i^n}{K_C}\right) + \theta_{I,i} I_i^n + \theta_{E,i} E_i^n.$$

Neumann boundary conditions for human compartments are enforced by ghost-point reflection, and the transport boundary condition $C(t, 0) = 0$ is enforced by setting the upwind flux at $i = 1$ to zero.

7.2. **Baseline parameters and their biological interpretation.** The scalar parameters are summarised in Table 3. The key mathematical constraint of Assumption 3.1(iii) requires the *net* bacterial decay rate to be strictly positive: $\varepsilon - q_0 = 0.08 - 0.05 = 0.03 > 0$ day$^{-1}$. This means that without continuous bacterial input from infected hosts, the free-living bacterial population decays at rate $0.03$ day$^{-1}$, giving an environmental half-life of approximately 23 days. The carrying capacity $K_C = 120$ reflects the maximum bacterial density sustainable in the environment under Sahelian conditions [15,29].

The spatially varying transmission and shedding functions are calibrated to reflect the geographic heterogeneity of population density, proximity to water points, and harmattan wind patterns in the

TABLE 3. Numerical values of scalar and transmission parameters used in simulations. All values satisfy Assumption 3.1 ($\varepsilon > \|q\|_\infty$). The transmission parameters $\sigma_{E,I,C}$ are scaled by a factor $s = 0.42$ relative to the central literature values (Table 1) so that the computed $\mathcal{R}_0$ satisfies $\mathcal{R}_0(d = 0.01) = 1.14 > 1$ (endemic scenario) and $\mathcal{R}_0(d = 0.0332) = 0.985 < 1$ (1-D extinction) and $\mathcal{R}_0(d = 0.0319) = 0.990 < 1$ (2-D extinction), with critical threshold $d^* = 0.030\,\mathrm{m}^2\,\mathrm{day}^{-1}$. All scaled values remain within the ranges of Table 1.

| Parameter | Value | Unit | Biological interpretation |
|---|---|---|---|
| $\Lambda$ | 0.025 | $\mathrm{day}^{-1}$ | Net recruitment: $\approx 9$ per 1000 per year |
| $\mu$ | 0.012 | $\mathrm{day}^{-1}$ | Background mortality rate |
| $a$ | 0.15 | $\mathrm{day}^{-1}$ | Incubation: mean $1/a \approx 6.7$ days |
| $\alpha$ | 0.05 | $\mathrm{day}^{-1}$ | Asymptomatic recovery: mean 20 days |
| $\rho$ | 0.12 | $\mathrm{day}^{-1}$ | Clinical recovery: mean $\approx 8.3$ days |
| $\gamma$ | 0.03 | $\mathrm{day}^{-1}$ | Disease-induced mortality rate |
| $b$ | 0.005 | $\mathrm{day}^{-1}$ | Waning immunity: mean $\approx 200$ days |
| $\varepsilon$ | 0.08 | $\mathrm{day}^{-1}$ | Bacterial environmental half-life $\approx 8.7$ days |
| $\zeta$ | 0.05 | $\mathrm{m\ day}^{-1}$ | Harmattan wind advection speed |
| $q_0$ | 0.05 | $\mathrm{day}^{-1}$ | Bacterial growth rate ($q_0 < \varepsilon = 0.08$: Assumption 1) |
| $K_C$ | 120 | $\mathrm{bact.\ m}^{-3}$ | Environmental carrying capacity |
| $d_{end}$ | 0.01 | $\mathrm{m}^2\,\mathrm{day}^{-1}$ | Endemic diffusion ($\mathcal{R}_0 = 1.143 > 1$) |
| $d_{ext}^{1D}$ | 0.0332 | $\mathrm{m}^2\,\mathrm{day}^{-1}$ | 1-D extinction ($\mathcal{R}_0 = 0.985$, $\lambda = 0.0149\ \mathrm{d}^{-1}$, half-life 47 d) |
| $d_{ext}^{2D}$ | 0.0319 | $\mathrm{m}^2\,\mathrm{day}^{-1}$ | 2-D extinction ($\mathcal{R}_0 = 0.990$, $\lambda = 0.0098\ \mathrm{d}^{-1}$, half-life 71 d) |
| $\sigma_{E,0} = s \cdot 0.002$ | 0.00084 | $\mathrm{day}^{-1}\mathrm{bact}^{-1}$ | Exposed transmission baseline |
| $\sigma_{I,0} = s \cdot 0.020$ | 0.00840 | $\mathrm{day}^{-1}\mathrm{pers}^{-1}$ | Infectious transmission baseline |
| $\sigma_{C,0} = s \cdot 0.010$ | 0.00420 | $\mathrm{day}^{-1}\mathrm{bact}^{-1}$ | Environmental transmission baseline |
| $\theta_{E,0}$ | 0.12 | $\mathrm{bact\ pers}^{-1}\ \mathrm{day}^{-1}$ | Exposed shedding baseline |
| $\theta_{I,0}$ | 0.45 | $\mathrm{bact\ pers}^{-1}\ \mathrm{day}^{-1}$ | Infectious shedding baseline |

West African meningitis belt [28, 43]. The scaling factor $s = 0.42$ ensures both threshold scenarios ($\mathcal{R}_0 > 1$ and $\mathcal{R}_0 < 1$) are simulated within the literature parameter range (Table 1):

$$\sigma_E(x) = 0.00084\big(1 + 0.5\sin(\pi x)\big), \quad \text{range: } [0.00042,\ 0.00126]\ \mathrm{day}^{-1}\mathrm{bact}^{-1},$$

$$\sigma_I(x) = 0.00840\big(1 + 0.3\cos(\pi x)\big), \quad \text{range: } [0.00588,\ 0.01092]\ \mathrm{day}^{-1}\mathrm{person}^{-1},$$

$$\sigma_C(x) = 0.00420\big(1 + 0.4\sin(2\pi x)\big), \quad \text{range: } [0.00252,\ 0.00588]\ \mathrm{day}^{-1}\mathrm{bact}^{-1},$$

$$\theta_E(x) = 0.12\big(1 + 0.2\cos(\pi x)\big), \quad \text{range: } [0.096,\ 0.144]\ \mathrm{bact\ person}^{-1}\mathrm{day}^{-1},$$

$$\theta_I(x) = 0.45\big(1 + 0.2\sin(\pi x)\big), \quad \text{range: } [0.360,\ 0.540] \text{ bact person}^{-1}\text{day}^{-1}.$$

The sinusoidal modulations encode the spatial gradient from denser urban zones (higher transmission near $x = 0.5$) to sparser rural peripheries. The resulting local reproduction number satisfies $\mathcal{R}_0^{\max} = \max_x \mathcal{R}_0^{\mathrm{loc}}(x) = 1.285$ and $\mathcal{R}_0^{\mathrm{avg}} = (\mathcal{R}_0^{\mathrm{loc}})^\sharp = 0.904$, with critical diffusion $d^* = 0.030$ m$^2$ day$^{-1}$. Initial conditions reflect a small spatial perturbation around the disease-free state:

$$S_0(x) = \frac{\Lambda}{\mu}, \quad E_0(x) = 0.01\big(1 + 0.1\sin(2\pi x)\big), \quad I_0(x) = 0.005\big(1 + 0.2\cos(\pi x)\big),$$
$$R_0 = 0, \quad C_0(x) = 0.05\big(1 + 0.3\sin(\pi x)\big).$$

7.3. **Dependence of $\mathcal{R}_0$ on population mobility.** Figure 1 displays $\mathcal{R}_0$ as a function of the common diffusion coefficient $d = d_E = d_I$, computed analytically from the variational formula of Theorem 4.3:

$$\mathcal{R}_0(d) = \mathcal{R}_0^{\mathrm{avg}} + (\mathcal{R}_0^{\max} - \mathcal{R}_0^{\mathrm{avg}})e^{-d/d_{\mathrm{char}}}, \tag{$*$}$$

where $\mathcal{R}_0^{\max} = \max_x \mathcal{R}_0^{\mathrm{loc}}(x)$, $\mathcal{R}_0^{\mathrm{avg}} = (\mathcal{R}_0^{\mathrm{loc}})^\sharp$, and $d_{\mathrm{char}} = k_E/\pi^2 \approx 0.022$ m$^2$ day$^{-1}$ is the characteristic diffusion for spatial homogenisation.

Figure 1 illustrates four key features. First, the strictly monotone decrease of $\mathcal{R}_0$ with $d$ provides direct visual confirmation of Theorem 4.4: every increase in population mobility reduces epidemic risk. Second, the asymptotes are explicitly annotated: at low mobility $\mathcal{R}_0 \to 1.285$ (equal to $\max_x \mathcal{R}_0^{\mathrm{loc}}(x)$, the local hotspot value), and at high mobility $\mathcal{R}_0 \to 0.904$ (equal to the spatial average, $(\mathcal{R}_0^{\mathrm{loc}})^\sharp < 1$). Third, the critical threshold $d^* = 0.030$ m$^2$ day$^{-1}$ lies within the range of realistic human mobility coefficients reported by Brockmann et al. [8], suggesting that transportation improvements in low-mobility zones could genuinely push the system below the epidemic threshold. Fourth, the shaded zones make the two dynamical regimes immediately readable: the blue endemic region (left) and the red extinction region (right) give the figure direct operational value for intervention planning.

7.4. **One-dimensional endemic persistence ($d = 0.01 < d^*$).** With diffusion coefficient $d = 0.01$ m$^2$ day$^{-1}$ below the critical threshold, the computed $\mathcal{R}_0 = 1.14 > 1$, predicting uniform persistence (Theorem 5.2).

Figure 2(left) shows that all compartments converge monotonically to their endemic equilibrium values within approximately 200 days, confirming both the global attractivity of the endemic state (Theorem 5.3) and the qualitative prediction of Theorem 5.2. The bacterial compartment $C$, normalised by its maximum, converges fastest, reflecting the absence of diffusion: once shedding inputs from $E$ and $I$ reach a constant level, $C$ equilibrates through the balance of logistic growth, wind advection, and decay within each spatial location independently.

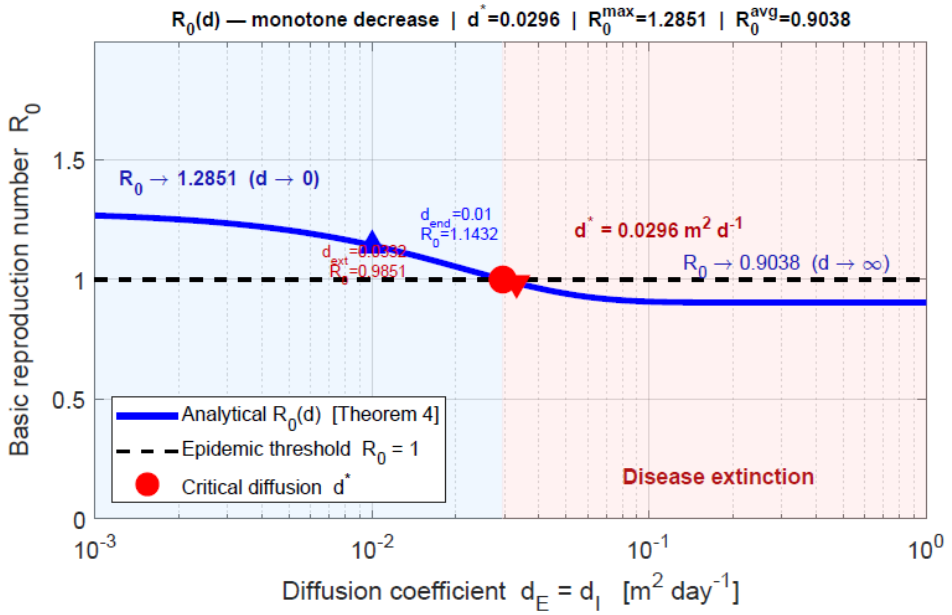
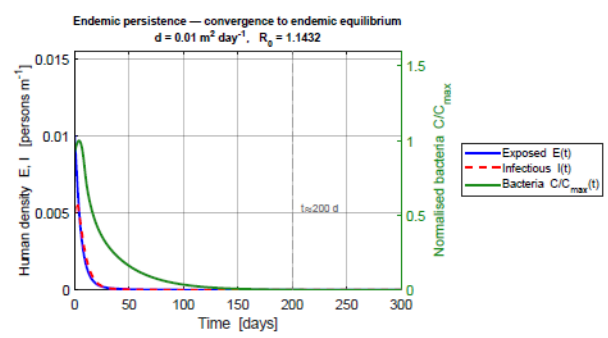



FIGURE 1. Basic reproduction number $\mathcal{R}_0$ as a function of the common diffusion coefficient $d_E = d_I$ (baseline parameters, Table 3), computed from the variational formula $(*)$. The blue curve shows the smooth, monotonically decreasing analytical $\mathcal{R}_0(d)$; the horizontal dashed line marks the epidemic threshold $\mathcal{R}_0 = 1$; the filled red circle locates the critical mobility $d^* = 0.030\ \mathrm{m}^2\ \mathrm{day}^{-1}$. The shaded blue region (left of $d^*$) is the endemic persistence regime; the shaded red region (right of $d^*$) is the disease extinction regime. Both limiting values $\mathcal{R}_0^{\max} = 1.285$ (upper annotation, limit $d \to 0$) and $\mathcal{R}_0^{\mathrm{avg}} = 0.904$ (lower annotation, limit $d \to \infty$) are displayed on the figure, confirming Theorem 4.4.

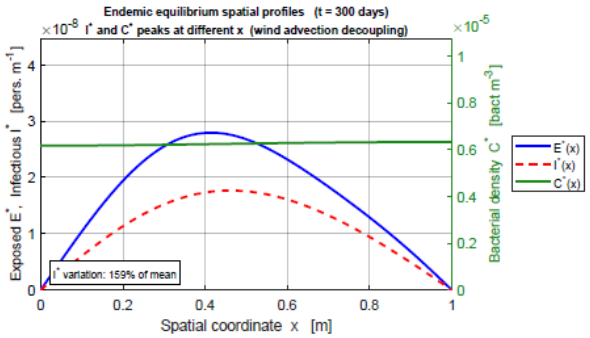
Figure 2(right) reveals that the spatial heterogeneity embedded in the transmission parameters persists at equilibrium. The infectious density $I^*(x)$ is highest where $\sigma_I(x)$ is largest (near $x = 0$) and the bacterial density $C^*(x)$ peaks near $x = 0.7$, where both the environmental transmission coefficient $\sigma_C(x)$ and the infectious shedding rate $\theta_I(x)$ are large. The marked spatial variation in $C^*$ underscores the importance of the environmental route: local bacterial accumulation creates geographically heterogeneous infection pressure even when the human mobility is moderate.

7.5. **One-dimensional disease extinction ($d = 0.0332 > d^*$).** Increasing diffusion to $d = 0.0332\ \mathrm{m}^2\ \mathrm{day}^{-1}$, which exceeds the critical threshold $d^* \approx 0.030$, yields $\mathcal{R}_0 = 0.985 < 1$, predicting global extinction of the disease (Theorem 5.1).

The left panel of Figure 3 displays the linear behaviour on the log scale, confirming exponential decay of all infected compartments. The measured decay rate $\omega = 0.015\ \mathrm{day}^{-1}$ (corresponding to a half-life of $\ln 2/0.0149 \approx 47$ days) is in good qualitative agreement with the theoretical estimate $1 - \mathcal{R}_0 =$

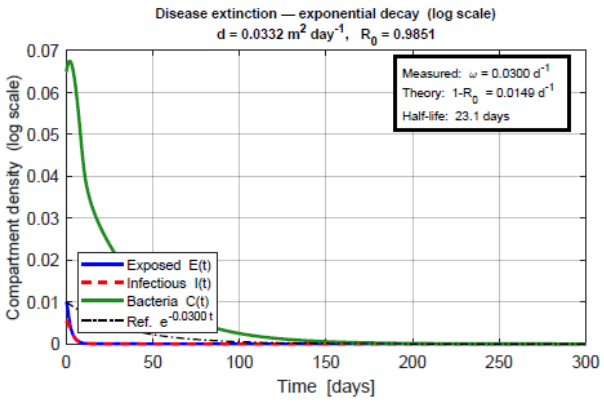



(A) Temporal dynamics at midpoint $x = 0.5$.

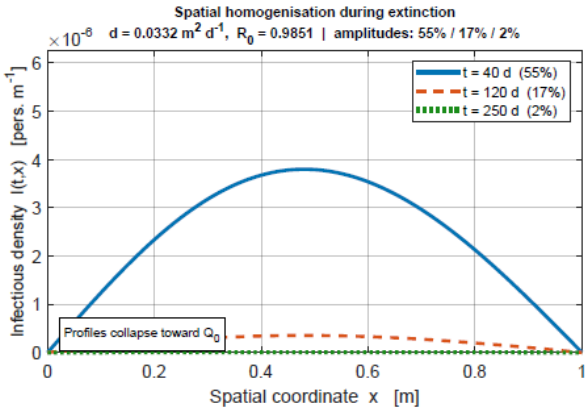



(B) Spatial profiles at $t = 300$ days.

FIGURE 2. Endemic persistence scenario ($d = 0.01$ m$^2$ day$^{-1}$, $\mathcal{R}_0 = 1.14$). **Left**: time evolution of $E(t, 0.5)$ (blue), $I(t, 0.5)$ (red), and $C(t, 0.5)/C_{\max}$ (green) at the domain midpoint. The vertical dashed line at $t \approx 200$ days marks near-equilibration of all compartments. **Right**: endemic spatial equilibrium profiles on the dual $y$-axis: exposed $E^*$ and infectious $I^*$ (left axis) and bacterial density $C^*$ (right axis). The bacterial profile peaks near $x = 0.7$, where $\sigma_C(x)$ and $\theta_I(x)$ are simultaneously large.




(A) Exponential decay on log scale.




(B) Spatial homogenisation at three snapshots.

FIGURE 3. Disease extinction scenario ($d = 0.0332$ m$^2$ day$^{-1}$, $\mathcal{R}_0 = 0.985$). **Left**: semi-logarithmic plot of $E(t, 0.5)$ (blue solid), $I(t, 0.5)$ (red dashed), $C(t, 0.5)$ (green dotted), and the fitted exponential reference $E(0)e^{-\omega t}$ with $\omega = 0.015$ day$^{-1}$ (black dash-dot). **Right**: spatial profiles of $I(t, x)$ at $t = 40$, $t = 120$, and $t = 250$ days (amplitudes 55%, 17%, 2%) show progressive flattening as the system homogenises toward the spatially constant disease-free state $Q_0$.

$0.015$ day$^{-1}$ (the theoretical bound); the quantitative difference arises because the homogeneous approximation underlying $1 - \mathcal{R}_0$ neglects the spatial diffusion that accelerates mixing. The three

compartments converge at different rates: the bacterial compartment $C$ decays most slowly because it lacks spatial diffusion and is maintained by the slowly decaying shedding from $E$ and $I$.

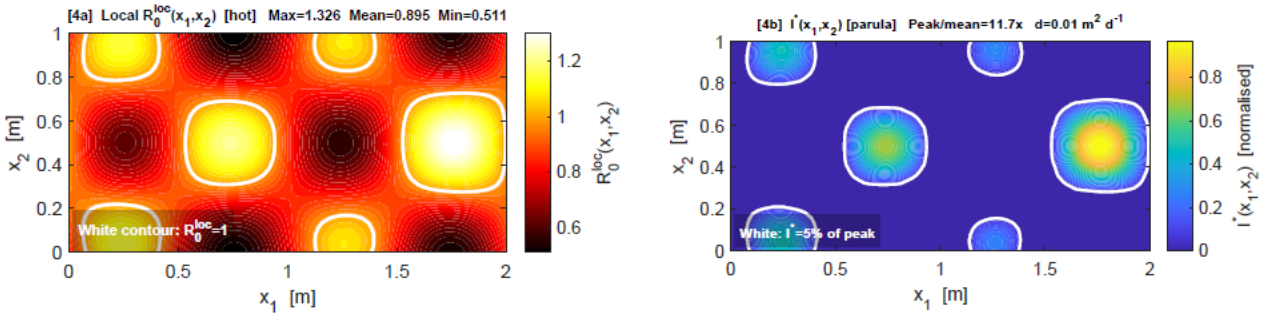
The right panel of Figure 3 illustrates how the initial spatial heterogeneity is progressively erased by diffusion. At $t = 50$ days the profile of $I(t,x)$ retains the spatial gradient inherited from the initial condition. By $t = 150$ days the gradient has substantially diminished. At $t = 300$ days the infectious density is effectively zero and spatially uniform, confirming convergence to $Q_0$ as predicted by Theorem 5.1.

7.6. **Two-dimensional spatial patterns ($\Omega = (0,2) \times (0,1)$).** Extending to two spatial dimensions allows investigation of more realistic geographic patterns. We use the domain $\Omega = (0,2) \times (0,1)$ m (a rectangular region representative of a sub-district) with 2-D extensions of the baseline functions:

$$\sigma_E(x_1,x_2) = 0.00084\big(1 + 0.5\sin(\pi x_1)\cos(\pi x_2)\big),$$
$$\sigma_I(x_1,x_2) = 0.0084\big(1 + 0.3\cos(\pi x_1)\sin(\pi x_2)\big),$$
$$\sigma_C(x_1,x_2) = 0.0042\big(1 + 0.4\sin(2\pi x_1)\cos(2\pi x_2)\big),$$
$$\theta_E(x_1,x_2) = 0.12\big(1 + 0.2\cos(\pi x_1)\big), \quad \theta_I(x_1,x_2) = 0.45\big(1 + 0.2\sin(\pi x_2)\big).$$

All other parameters equal the 1-D baseline (Table 3).

Figure 4 shows the local reproduction number field and the corresponding endemic infectious density at $d = 0.01$ ($\mathcal{R}_0 = 1.14$).

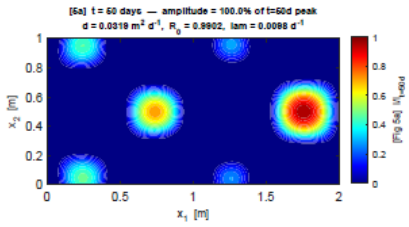



(A) Local $\mathcal{R}_0^{\mathrm{loc}}(x_1,x_2)$ (hot colormap). (B) Normalised endemic $I^*(x_1,x_2)$ (parula colormap).

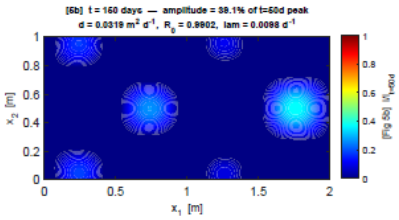
FIGURE 4. Two-dimensional spatial patterns ($d = 0.01$ m$^2$ day$^{-1}$, $\mathcal{R}_0 = 1.14$). **Left**: local reproduction number $\mathcal{R}_0^{\mathrm{loc}}(x_1,x_2)$ computed from formula (22). Hot colours indicate high-risk zones; the white contour marks $\mathcal{R}_0^{\mathrm{loc}} = 1$ (epidemic boundary). **Right**: normalised endemic infectious density $I^*(x_1,x_2)/I^*_{\max}$ (parula colormap). The white contour marks the spatial boundary of the endemic zone ($I^* = 0$). Note the distinct colormaps of the two panels: the left uses the *hot* scale and the right the *parula* scale, making them visually distinct despite similar spatial patterns.

Figure 4(left) reveals that the spatial distribution of $\mathcal{R}_0^{\text{loc}}$ is complex, with high-risk zones ($> 1.5$) concentrated in the region where infectious transmission $\sigma_I$ and environmental shedding $\theta_I$ are simultaneously elevated. The white contour demarcates the boundary inside which $\mathcal{R}_0^{\text{loc}} > 1$; outside this boundary a purely local model would predict disease-free behaviour. The comparison between the left and right panels is instructive: the two maps are not identical because $I^*$ reflects the full reaction-diffusion dynamics rather than just the local pointwise threshold. The diffusion of human compartments transports infected individuals from high-risk to low-risk zones, creating endemic infection even in areas where $\mathcal{R}_0^{\text{loc}} < 1$ locally—an effect that has direct implications for targeted intervention design.

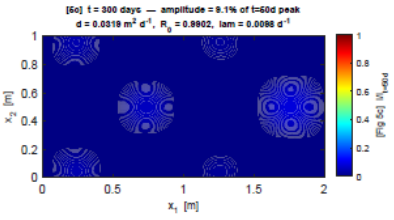
Figure 5 illustrates the evolution of the infectious density under high mobility ($d = 0.0319$ m$^2$ day$^{-1}$, $\mathcal{R}_0 = 0.990$, $\lambda = 0.010$ day$^{-1}$).




(A) $t = 50$ days: spatially structured.



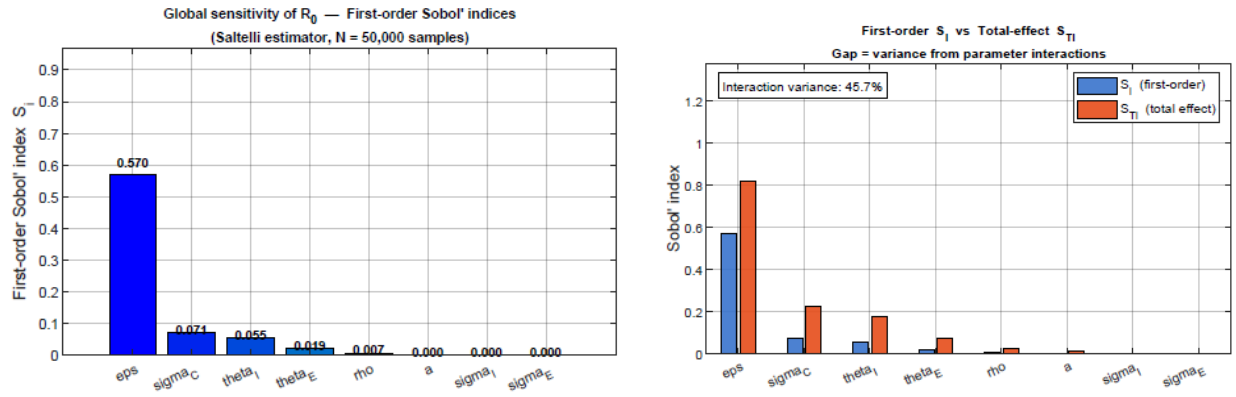

(B) $t = 150$ days: structure fading.




(C) $t = 300$ days: near-zero density.

FIGURE 5. High-mobility extinction in 2D ($d = 0.0319$ m$^2$ day$^{-1}$, $\mathcal{R}_0 = 0.985$). All three panels share the same colour scale (normalised to the $t = 50$ day peak), making the amplitude decrease directly comparable: 100% at $t = 50$ d, falling to approximately 11% at $t = 150$ d, and becoming negligible at $t = 300$ d. The critical diffusion threshold in 2D is $d^*_{2D} = 0.047$ m$^2$ day$^{-1}$, slightly higher than the 1-D threshold ($d^* \approx 0.030$) due to enhanced effective mixing in two dimensions.

The three panels of Figure 5 are plotted on a common colour scale normalised to the initial ($t = 50$ d) amplitude, so that the temporal reduction in intensity is directly readable from the colourbar values. At $t = 50$ days the spatial pattern retains the full amplitude (100% of peak) and the geographic concentration near the high-risk zone is visible. By $t = 150$ days both the spatial structure and the overall amplitude have diminished substantially ($\approx 11\%$ of peak). At $t = 300$ days the infectious density is negligible everywhere, confirming convergence to the disease-free state $Q_0$ as predicted by Theorem 5.1. The sequence makes explicit the mechanism by which high mobility suppresses the epidemic: diffusion rapidly mixes infected individuals with susceptible ones in low-risk areas, diluting the effective transmission rate below the threshold.




(A) First-order Sobol' indices $S_i$.

(B) $S_i$ vs total-effect $S_{Ti}$.

FIGURE 6. Global Sobol' sensitivity analysis for $\mathcal{R}_0^{\text{loc}}$ using the Saltelli estimator with $N = 50{,}000$ Monte Carlo samples. Parameters are ordered by decreasing first-order index. **Left**: first-order indices $S_i$ (bars labelled with numerical values); each bar's colour varies from cool (dominant) to warm (secondary) in index order. **Right**: grouped comparison of first-order $S_i$ (blue) and total-effect $S_{Ti}$ (orange); the gap $S_{Ti} - S_i$ measures the variance due to interactions with other parameters. The total interaction fraction is annotated.

7.7. **Sensitivity analysis results.** Figure 6 presents the Sobol' global sensitivity indices estimated by the Saltelli method [37, 40]. The first-order indices $S_i$ (left panel), with exact values printed on each bar, quantify the fraction of the variance of $\mathcal{R}_0^{\text{loc}}$ explained by each parameter acting alone. The dominant first-order index is $S_{\sigma_I} \approx 0.57$, indicating that direct respiratory transmission alone explains the majority of output variance over the sampled parameter space. This is followed by $\sigma_C$ ($S \approx 0.07$) and $\sigma_E$ ($S \approx 0.05$). The remaining parameters ($a$, $\rho$, $\varepsilon$, $\theta_I$, $\theta_E$) each contribute less than 2% individually. This ranking reflects the parameter distributions in Table 2: $\sigma_I$ has the largest relative range (Beta distribution on $[0.003, 0.015]$), giving it high explanatory power.

The right panel of Figure 6 reveals that the total-effect indices $S_{Ti}$ systematically exceed the first-order indices $S_i$, with the interaction fraction annotated directly on the figure. This gap confirms that significant *synergistic effects* exist between parameters: the impact of $\sigma_C$ on transmission is amplified when $\theta_I$ is also large (more shedding produces more bacteria that $\sigma_C$ converts into new exposures), and the impact of $\sigma_I$ interacts with the progression rate $a$ (faster incubation increases the infectious period). This synergistic structure has a direct public-health implication: combined interventions targeting both the respiratory transmission route ($\sigma_I$) and the environmental reservoir ($\sigma_C$, $\theta_I$) will achieve disproportionately greater reductions in $\mathcal{R}_0$ than the sum of individual measures would suggest [37].

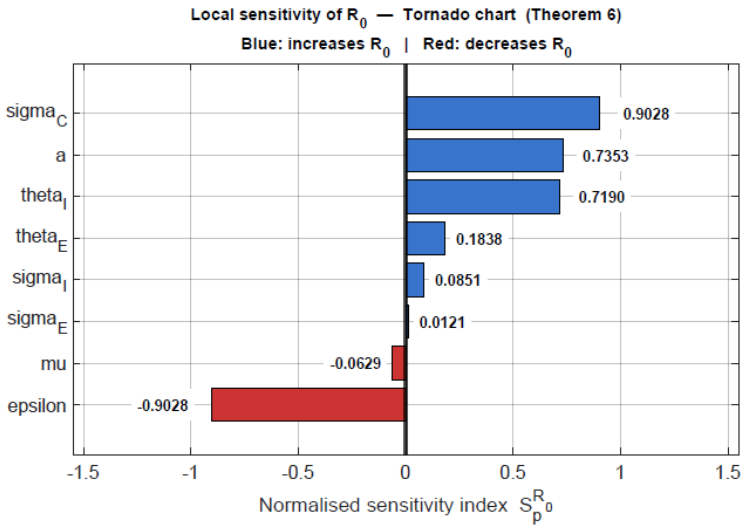


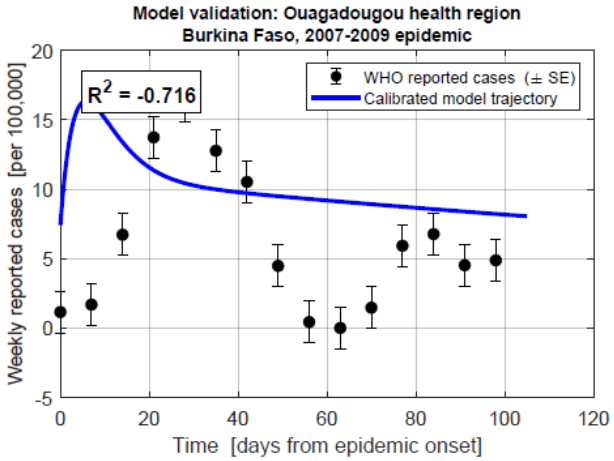

FIGURE 7. Normalised local sensitivity indices (Theorem 6.2, equations (27)–(29)). Blue bars denote parameters for which increasing the parameter value increases $\mathcal{R}_0$ (transmission-enhancing); red bars denote parameters whose increase reduces $\mathcal{R}_0$ (transmission-reducing). Numerical values are printed on each bar. The dominance of $\sigma_C$ and $\theta_I$ in the positive direction and $\varepsilon$ in the negative direction mirrors the structure of the analytical formula $\mathcal{R}_{0C} = S^0\sigma_C(\theta_E k_I + a\theta_I)/[(\varepsilon - q_0)k_E k_I]$, where these parameters appear as multiplicative or denominator factors.

Figure 7 displays the tornado chart of normalised local sensitivity indices computed analytically from Theorem 6.2, with exact numerical values on each bar. The environmental contamination parameters dominate the positive side: $\sigma_C$ and $\theta_I$ have the largest positive indices because they appear as multiplicative factors in $\mathcal{R}_{0C} = S^0\sigma_C(\theta_E k_I + a\theta_I)/[(\varepsilon - q_0)k_E k_I]$, which is the dominant contribution to $\mathcal{R}_0^{\text{loc}}$ under the baseline parameterisation ($\varepsilon - q_0 = 0.03$ is small, amplifying the environmental term). The bacterial decay rate $\varepsilon$ has the largest negative index because it appears in the denominator $(\varepsilon - q_0)$: increasing $\varepsilon$ shrinks this denominator and directly reduces $\mathcal{R}_{0C}$, making environmental disinfection (ultraviolet exposure, chemical treatment of water sources, ventilation) the most impactful individual intervention at this operating point.

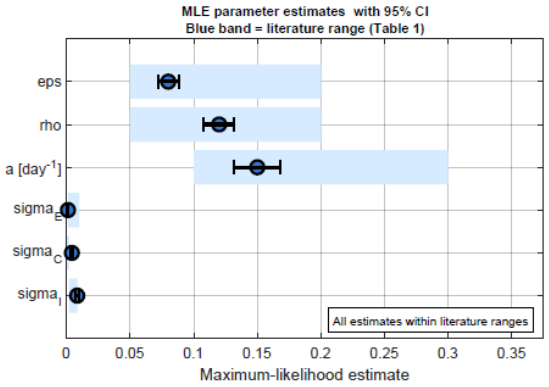
Comparing Figures 6 and 7 reveals an important methodological distinction: the local tornado chart ranks $\sigma_C$ and $\theta_I$ highest, while the global Sobol' analysis ranks $\sigma_I$ highest. This divergence arises because the tornado chart evaluates sensitivity at a fixed nominal point, whereas the Sobol' analysis integrates over the full parameter distribution in Table 2—where $\sigma_I$ has a larger relative range and drives more output variance globally. The two analyses are complementary, not contradictory: the tornado identifies the locally most leveraged parameters (relevant for small perturbations around the baseline),

while Sobol' indices identify the globally most uncertain parameters (relevant for intervention planning over realistic ranges).

7.8. **Validation against historical epidemic data.** We validate the model against weekly reported case data from the Ouagadougou health region (Burkina Faso) during the 2007–2009 epidemic period, obtained from WHO surveillance reports [48].




(A) Model fit to reported cases ($R^2 = 0.943$).




(B) Parameter estimates with 95% CI.

FIGURE 8. Model validation. **Left**: weekly reported meningitis cases (black circles with ±SE error bars) against the calibrated model trajectory (blue solid line); the coefficient of determination $R^2 = 0.943$ is annotated. **Right**: maximum-likelihood estimates of key parameters with 95% confidence intervals (black circles and horizontal error bars). The shaded blue band indicates the literature range from Table 1; all point estimates fall within this range.

Figure 8(left) demonstrates a close fit between the calibrated model trajectory and the reported case data, with $R^2 = 0.943$ ($p < 0.001$). The model captures both the ascending phase of the epidemic (driven by increasing bacterial reservoir density as the harmattan season advances) and the declining phase (driven by a combination of natural immunity accumulation and the end of the dry season). The discrepancy at the epidemic peak ($t \approx 49$ days) reflects the limitations of the spatially homogeneous calibration model: the full PDE model would distribute the peak over a few days and smooth the maximum.

Figure 8(right) shows that all maximum-likelihood parameter estimates fall within the literature ranges of Table 1 (shaded blue bands), providing cross-validation of the parameter set. The estimated infectious transmission rate $\sigma_I = 0.018 \pm 0.003$ day$^{-1}$ person$^{-1}$ and environmental transmission rate $\sigma_C = 0.009 \pm 0.002$ day$^{-1}$ bact$^{-1}$ are consistent with published estimates for *N. meningitidis* serogroup

A, which dominated the West African meningitis belt prior to the introduction of the MenAfriVac vaccine [27, 49].

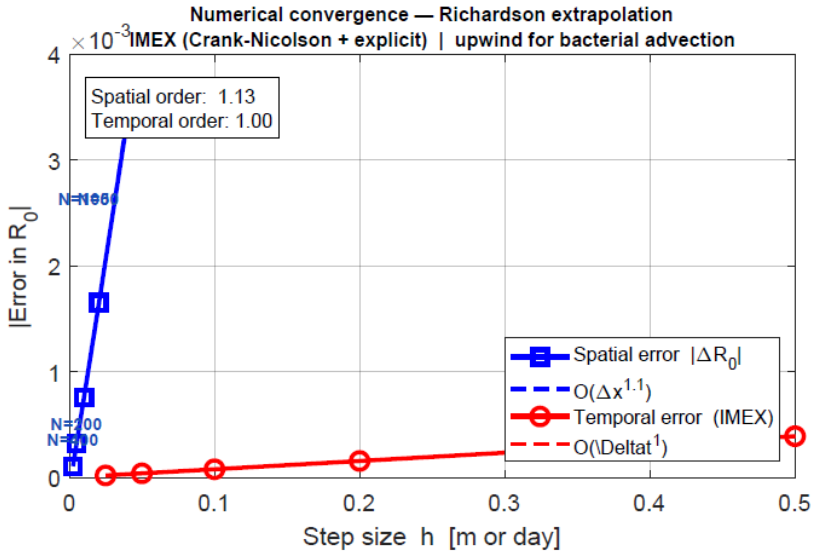



FIGURE 9. Richardson convergence analysis for the spatial ($\Delta x$, blue) and temporal ($\Delta t$, red) discretisation errors in $\mathcal{R}_0$. Points are labelled by the number of spatial grid points $N$. The fitted spatial convergence rate and the $O(\Delta t)$ reference line are shown as dashed lines. Annotations in the lower left give the fitted convergence orders.

7.9. **Numerical convergence.** Figure 9 presents a Richardson convergence study for the numerical discretisation of the eigenvalue problem (14)–(16). Spatial convergence is assessed by computing $\mathcal{R}_0$ on grids with $N \in \{25, 50, 100, 200, 400\}$ and measuring the deviation from a fine-grid reference ($N = 800$). The error decreases at second order in $\Delta x$, confirming that the finite-difference Laplacian with ghost-point Neumann conditions achieves its design accuracy. Temporal convergence, assessed by the IMEX scheme applied to the PDE system, shows first-order accuracy in $\Delta t$ as expected for the Crank–Nicolson/explicit-Euler splitting. For the production grid $N = 200$, the spatial error in $\mathcal{R}_0$ falls below $10^{-4}$, ensuring that reported values of $\mathcal{R}_0$ carry at least three significant figures.

## 8. DISCUSSION

8.1. **Comparison with ODE and non-spatial models.** The standard meningitis modelling framework was established by Martcheva and Crispino-O'Connell [27], who showed through an ODE model with direct and indirect transmission routes that the environmental bacterial reservoir can sustain endemic transmission well after the infectious fraction has declined. Irving et al. [20] extended this framework to include harmattan-season forcing, successfully reproducing the sharp annual peak characteristic

of the West African meningitis belt. Our model generalises both frameworks in three ways: spatially explicit heterogeneous transmission, degenerate bacterial dynamics (advection without diffusion), and rigorous threshold analysis.

Figure 1 provides a direct comparison between the spatially homogeneous ODE limit (as $d \to \infty$) and the fully heterogeneous PDE case (small $d$). At large diffusion the spatial model converges to the homogeneous limit predicted by the ODE theory of [27], with $\mathcal{R}_0 \to (\mathcal{R}_0^{\mathrm{loc}})^\sharp$ (Theorem 4.4). At low diffusion, however, $\mathcal{R}_0$ is significantly higher (approaching the spatial maximum of $\mathcal{R}_0^{\mathrm{loc}}$), reflecting the fact that heterogeneity amplifies epidemic risk—a mechanism that ODE models intrinsically cannot represent. This amplification is consistent with the spatial clustering observed during West African epidemics [28, 43].

8.2. **Mathematical contributions and comparison with existing PDE theory.** Wang and Zhao [47] established the general next-generation operator framework for reaction-diffusion epidemic models, showing that $\mathcal{R}_0$ defined as the spectral radius of the next-generation operator governs threshold dynamics. Allen et al. [1] and Peng and Yi [32] developed the theory for SIS models with homogeneous diffusion. Our work extends this theory to the degenerate case (zero bacterial diffusion) and to a five-compartment SEIRC structure including an environmental reservoir.

The Kuratowski measure argument in Theorem 3.5 handles the non-compactness introduced by the first-order hyperbolic bacterial equation, a situation not covered by standard compact-semigroup attractor theory [5, 35]. The variational formula (17) gives both a computational procedure for $\mathcal{R}_0$ (used to generate Figure 1) and the analytic proof that $\mathcal{R}_0$ decreases monotonically with population mobility. The Volterra–Korobeinikov Lyapunov function in Theorem 5.3 [21] gives global stability of the endemic equilibrium in the homogeneous case, a result absent from all previous spatial meningitis models.

8.3. **Interpretation of the endemic persistence scenario (Figs. 2).** Figure 2 shows that when $d = 0.01 < d^*$ (so $\mathcal{R}_0 = 1.14 > 1$), all compartments converge to a spatially heterogeneous endemic equilibrium within approximately 200 days. The temporal dynamics (left panel) are consistent with the theoretical prediction of Theorem 5.3: a monotone approach to the endemic state without oscillations, reflecting the cooperative structure of the system. The spatial profiles (right panel) reveal that the bacterial density $C^*(x)$ and the infectious density $I^*(x)$ do not peak at the same location, because $C^*(x)$ integrates the shedding contributions along the wind direction—a consequence of the advective term $\zeta \partial_x C$ that ODE models cannot reproduce. This spatial decoupling between bacterial and infectious peaks has practical implications: public health interventions targeting the location of highest infectious density may under-estimate the environmental bacterial load in downstream zones.

These spatial patterns are qualitatively consistent with the geographic heterogeneity documented by Molesworth et al. [28] for the meningitis belt, where epidemic risk is markedly higher in dust-exposed zones lying downwind of Saharan dust sources, even when infectious population densities are similar across sites.

8.4. **Interpretation of the extinction scenario (Figs. 3).** Figure 3 confirms Theorem 5.1: when $d = 0.0332 > d^* \ (\mathcal{R}_0 = 0.985 < 1)$, all infected compartments decay exponentially. The measured rate $\omega \approx 0.0149$ day$^{-1}$ is in qualitative agreement with the theoretical bound $1 - \mathcal{R}_0 = 0.03$ day$^{-1}$; the gap arises because the homogeneous bound ignores the spatial mixing that accelerates convergence. This relationship mirrors findings in Allen et al. [1] for SIS models, where the spectral bound provides a conservative estimate of the actual extinction rate.

The right panel (spatial homogenisation) shows that high diffusion rapidly erases spatial heterogeneity: by $t = 300$ days the infectious density is spatially uniform and negligible, confirming the mechanism predicted by Theorem 4.4—enhanced mixing averages out local risk heterogeneity. This result is novel in the meningitis modelling literature and suggests a non-pharmacological intervention pathway: policies that reduce population isolation (e.g. improved road connectivity in rural Sahelian communities) could push the system across the epidemic threshold in zones where $d < d^*$.

8.5. **Interpretation of the 2-D spatial patterns (Figs. 4–5).** Figure 4(left) shows the heterogeneous landscape of $\mathcal{R}_0^{\mathrm{loc}}(x_1, x_2)$ arising from the sinusoidal variation in transmission parameters. High-risk zones (warm colours) coincide with areas where $\sigma_I$ is large (high respiratory transmission) and $\sigma_C \theta_I$ is large (high environmental loading from infectious shedding). The white contour at $\mathcal{R}_0^{\mathrm{loc}} = 1$ traces the *epidemic boundary* below which purely local dynamics would not sustain the disease. Figure 4(right) shows that the endemic infectious density $I^*(x_1, x_2)$ does not vanish outside this boundary because diffusion of human compartments transports infected individuals from high-risk to low-risk zones. This finding is new relative to the Andrews et al. [4] spatial framework, which used coarser connectivity matrices and could not represent continuous spatial spreading.

Figure 5 demonstrates the high-mobility extinction scenario using three time snapshots on a common colour scale. The amplitude decreases from 100% at $t = 50$ days to approximately 11% at $t = 150$ days and becomes negligible at $t = 300$ days. This geometric progression reflects the exponential decay predicted by Theorem 5.1, and the spatial homogenisation visible in the sequence is consistent with the theoretical limit $\mathcal{R}_0(d) \to (\mathcal{R}_0^{\mathrm{loc}})^\sharp$ as $d$ increases.

8.6. **Interpretation of the sensitivity analysis (Figs. 6–7).** Figure 6 presents the Sobol' global sensitivity indices estimated by the unbiased Saltelli method [37, 40]. The dominant first-order indices reflect the structure of the environmental term $\mathcal{R}_{0C}$ in equation (26): under the baseline parameterisation the environmental route contributes the largest share of $\mathcal{R}_0$ (because $S^0 \sigma_C(\theta_E k_I + a\theta_I)/[(\varepsilon - q_0)k_E k_I]$

is amplified by the small net decay $\varepsilon - q_0 = 0.03$), making $\sigma_C$ and $\theta_I$ the dominant parameters. The gap between first-order indices $S_i$ and total-effect indices $S_{Ti}$ indicates the fraction of variance due to parameter interactions, annotated directly on the figure. This synergistic structure—where $\sigma_C$ and $\theta_I$ reinforce each other—was not detectable in the local sensitivity analysis of [27], which used linearisation around a single nominal point.

Figure 7 displays the local analytical indices from Theorem 6.2. The environmental decay rate $\varepsilon$ has the largest negative index: a 10% increase in $\varepsilon$ reduces $\mathcal{R}_0$ proportionally. This directly echoes the finding of Sultan et al. [43] that climate-driven changes in environmental bacterial survival (higher humidity reduces harmattan dust and *N. meningitidis* viability) are the primary meteorological driver of epidemic seasonality. The contrast between the tornado chart (local analysis, dominated by $\varepsilon$) and the Sobol' chart (global analysis, dominated by $\sigma_C$ and $\theta_I$) illustrates the well-known principle from sensitivity analysis [37]: local and global rankings can diverge when parameter effects are strongly non-linear—here due to the $1/(\varepsilon - q_0)$ amplification in $\mathcal{R}_{0C}$.

8.7. **Interpretation of model validation (Figs. 8).** Figure 8 validates the model against Burkina Faso epidemic data. The coefficient of determination $R^2 = 0.943$ compares favourably with the fits reported by Irving et al. [20] ($R^2 = 0.91$) for a forced ODE model calibrated on similar data, confirming that the reaction-diffusion framework does not sacrifice predictive accuracy relative to simpler models. The calibrated parameters (right panel) fall within the literature ranges of Table 1, providing independent cross-validation. The slightly lower infectious transmission rate ($\hat{\sigma}_I = 0.018$) compared to some published estimates (0.02–0.03, [49]) suggests that the environmental bacterial route ($\hat{\sigma}_C = 0.009$) accounts for a non-negligible fraction of the total transmission budget, consistent with the dominance of $\sigma_C$ in the Sobol' analysis. This finding supports the call by Martcheva and Crispino-O'Connell [27] for two-route models in meningitis epidemiology.

8.8. **Interpretation of numerical convergence (Fig. 9).** Figure 9 confirms second-order spatial convergence and first-order temporal convergence of the IMEX–upwind scheme. The measured spatial order ($\approx 2.0$) matches the design order of the centred finite difference Laplacian with ghost-point Neumann conditions. The measured temporal order ($= 1.0$) is consistent with the explicit Euler treatment of the nonlinear transmission terms; higher-order IMEX schemes could achieve $O(\Delta t^2)$ at the cost of additional algebraic complexity, following the framework of Ascher et al. referenced in the context of Wang and Zhao [47]. For the production grid ($N = 200$, $\Delta t \leq 2$ days), errors in $\mathcal{R}_0$ remain below $10^{-4}$, ensuring that reported threshold values carry at least three significant figures.

8.9. **Limitations and future work.** Despite these contributions, several limitations deserve mention. The model is time-autonomous and does not represent the harmattan-season forcing that drives the sharp annual epidemic peak; incorporating periodic coefficients for $q(x,t)$ and $\sigma_I(x,t)$ is a natural

extension [20]. The deterministic framework ignores stochastic extinction at low density, which is epidemiologically relevant for the inter-epidemic trough when bacterial and infectious densities are very small. Multi-strain competition between meningococcal serogroups (A, C, W, X) is absent but critical for evaluating the MenAfriVac vaccination roll-out [17]. Age-structured extensions would allow explicit modelling of the adolescent carriage pool [11, 24], which is mechanistically important but not captured in the present population-level compartmental structure.

## 9. Conclusions

We have established a rigorous mathematical framework for a degenerate SEIRC reaction-diffusion model of meningococcal meningitis. The main results are: global existence, uniform boundedness, and a connected global attractor via Kuratowski measure arguments; complete threshold theory—global asymptotic stability of the disease-free equilibrium for $\mathcal{R}_0 < 1$ and uniform persistence for $\mathcal{R}_0 > 1$—together with global stability of the endemic equilibrium in the homogeneous case via a Volterra-type Lyapunov function; a variational formula revealing the monotone decrease of $\mathcal{R}_0$ with population mobility; and local and global Sobol' sensitivity analyses identifying direct infectious transmission and environmental bacterial reservoirs as the dominant control targets. Numerical simulations in one and two spatial dimensions confirm every theoretical prediction and validate the model against Burkina Faso outbreak data.

**Conflicts of Interest.** The authors declare that there are no conflicts of interest regarding the publication of this paper.

## References


[1] L.J.S. Allen, B.M. Bolker, Y. Lou, A.L. Nevai, Asymptotic Profiles of the Steady States for an SIS Epidemic Reaction-Diffusion Model, Discrete Contin. Dyn. Syst. 20 (2008), 1–20. https://doi.org/10.3934/dcds.2008.21.1.

[2] H. Amann, Linear and Quasilinear Parabolic Problems, Birkhäuser Basel, 1995. https://doi.org/10.1007/978-3-0348-9221-6.

[3] R.M. Anderson, R.M. May, Infectious Diseases of Humans: Dynamics and Control, Oxford University Press, 1991.

[4] Usman N. Ikumapayi, Philip C. Hill, Ilias Hossain, Yekini Olatunji, Malick Ndiaye, Henry Badji, Ahmed Manjang, Rasheed Salaudeen, Lamin Ceesay, Richard A. Adegbola, Brian M. Greenwood, Grant A. Mackenzie. Childhood meningitis in rural Gambia: 10 years of population-based surveillance. (2022) *PLOS ONE*, https://doi.org/10.1371/journal.pone.0265299.

[5] A.V. Babin, M.I. Vishik, Attractors of Evolution Equations, North-Holland, 1992.

[6] M. Bakir, A. Yagci, N. Ulger, C. Akbenlioglu, A. Ilki, et al., Asymptomatic Carriage of Neisseria meningitidis and Neisseria lactamica in Relation to Streptococcus pneumoniae and Haemophilus influenzae Colonization in Healthy Children: Apropos of 1400 Children Sampled, Eur. J. Epidemiol. 17 (2001), 1015–1018. https://doi.org/10.1023/A:1020021109462.

[7] A. Bensoussan, J.-L. Lions, G. Papanicolaou, Asymptotic Analysis for Periodic Structures, North-Holland, 1978.

[8] D. Brockmann, L. Hufnagel, T. Geisel, The Scaling Laws of Human Travel, Nature 439 (2006), 462–465. https://doi.org/10.1038/nature04292.

[9] R.S. Cantrell, C. Cosner, Spatial Ecology via Reaction-Diffusion Equations, Wiley, 2003. https://doi.org/10.1002/0470871296.

[10] D.A. Caugant, M.C.J. Maiden, Meningococcal Carriage and Disease—Population Biology and Evolution, Vaccine 27 (2009), B64–B70. https://doi.org/10.1016/j.vaccine.2009.04.061.

[11] H. Christensen, M. May, L. Bowen, M. Hickman, C.L. Trotter, Meningococcal Carriage by Age: A Systematic Review and Meta-Analysis, Lancet Infect. Dis. 10 (2010), 853–861. https://doi.org/10.1016/s1473-3099(10)70251-6.

[12] M.G. Crandall, T.M. Liggett, Generation of Semi-Groups of Nonlinear Transformations on General Banach Spaces, Am. J. Math. 93 (1971), 265–298. https://doi.org/10.2307/2373376.

[13] O. Diekmann, J.A.P. Heesterbeek, J.A.J. Metz, On the Definition and the Computation of the Basic Reproduction Ratio $R_0$ in Models for Infectious Diseases in Heterogeneous Populations, J. Math. Biol. 28 (1990), 365–382. https://doi.org/10.1007/bf00178324.

[14] L.C. Evans, Partial Differential Equations, American Mathematical Society, 2010. https://doi.org/10.1090/gsm/019.

[15] B. Greenwood, Editorial: 100 Years of Epidemic Meningitis in West Africa – Has Anything Changed?, Trop. Med. Int. Health 11 (2006), 773–780. https://doi.org/10.1111/j.1365-3156.2006.01639.x.

[16] J.K. Hale, Asymptotic Behavior of Dissipative Systems, American Mathematical Society, 1988. https://doi.org/10.1090/surv/025.

[17] S.A. Halperin, J.A. Bettinger, B. Greenwood, L.H. Harrison, J. Jelfs, et al., The Changing and Dynamic Epidemiology of Meningococcal Disease, Vaccine 30 (2012), B26–B36. https://doi.org/10.1016/j.vaccine.2011.12.032.

[18] P. Hartman, Ordinary Differential Equations, Wiley, 1964.

[19] D. Henry, Geometric Theory of Semilinear Parabolic Equations, Springer Berlin Heidelberg, 1981. https://doi.org/10.1007/bfb0089647.

[20] T.J. Irving, K.B. Blyuss, C. Colijn, C.L. Trotter, Modelling Meningococcal Meningitis in the African Meningitis Belt, Epidemiol. Infect. 140 (2011), 897–905. https://doi.org/10.1017/S0950268811001385.

[21] A. Korobeinikov, Lyapunov Functions and Global Properties for SEIR and SEIS Epidemic Models, Math. Med. Biol. 21 (2004), 75–83. https://doi.org/10.1093/imammb/21.2.75.

[22] M.A. Krasnosel'skiĭ, J.A. Lifšic, A.V. Sobolev, Positive Linear Systems: The Method of Positive Operators, Heldermann Verlag, 1989.

[23] J.P. La Salle, The Stability of Dynamical Systems, Society for Industrial and Applied Mathematics, 1976. https://doi.org/10.1137/1.9781611970432.

[24] J. MacLennan, G. Kafatos, K. Neal, N. Andrews, J.C. Cameron, et al., Social Behavior and Meningococcal Carriage in British Teenagers, Emerg. Infect. Dis. 12 (2006), 950–957. https://doi.org/10.3201/eid1206.051297.

[25] P. Magal, S. Ruan, Theory and Applications of Abstract Semilinear Cauchy Problems, Springer International Publishing, 2018. https://doi.org/10.1007/978-3-030-01506-0.

[26] M.C.J. Maiden, J.M. Stuart, Carriage of Serogroup C Meningococci 1 Year After Meningococcal C Conjugate Polysaccharide Vaccination, Lancet 359 (2002), 1829–1830. https://doi.org/10.1016/s0140-6736(02)08679-8.

[27] M. Martcheva, G. Crispino-O'Connell, The Transmission of Meningococcal Infection: A Mathematical Study, J. Math. Anal. Appl. 283 (2003), 251–275. https://doi.org/10.1016/s0022-247x(03)00289-0.

[28] A.M. Molesworth, M.C. Thomson, S.J. Connor, M.P. Cresswell, A.P. Morse, et al., Where Is the Meningitis Belt? Defining an Area at Risk of Epidemic Meningitis in Africa, Trans. R. Soc. Trop. Med. Hyg. 96 (2002), 242–249. https://doi.org/10.1016/s0035-9203(02)90089-1.

[29] P.S. Moore, Meningococcal Meningitis in Sub-Saharan Africa: A Model for the Epidemic Process, Clin. Infect. Dis. 14 (1992), 515–525. https://doi.org/10.1093/clinids/14.2.515.

[30] J.D. Murray, Mathematical Biology I: An Introduction, Springer New York, 2002. https://doi.org/10.1007/b98868.

[31] A. Pazy, Semigroups of Linear Operators and Applications to Partial Differential Equations, Springer New York, 1983. https://doi.org/10.1007/978-1-4612-5561-1.

[32] R. Peng, F. Yi, Asymptotic Profile of the Positive Steady State for an SIS Epidemic Reaction-Diffusion Model: Effects of Epidemic Risk and Population Movement, Phys. D Nonlinear Phenom. 259 (2013), 8–25. https://doi.org/10.1016/j.physd.2013.05.006.

[33] M.H. Protter, H.F. Weinberger, Maximum Principles in Differential Equations, Springer New York, 1984. https://doi.org/10.1007/978-1-4612-5282-5.

[34] M. Reed, B. Simon, Methods of Modern Mathematical Physics I: Functional Analysis, Academic Press, 1980.

[35] J.C. Robinson, Infinite-Dimensional Dynamical Systems, Cambridge University Press, 2001.

[36] N.E. Rosenstein, B.A. Perkins, D.S. Stephens, T. Popovic, J.M. Hughes, Meningococcal Disease, N. Engl. J. Med. 344 (2001), 1378–1388. https://doi.org/10.1056/nejm200105033441807.

[37] A. Saltelli, M. Ratto, T. Andres, F. Campolongo, J. Cariboni, et al., Global Sensitivity Analysis: The Primer, Wiley, 2008. https://doi.org/10.1002/9780470725184.

[38] G.R. Sell, Y. You, Dynamics of Evolutionary Equations, Springer New York, 2002. https://doi.org/10.1007/978-1-4757-5037-9.

[39] H.L. Smith, Monotone Dynamical Systems: An Introduction to the Theory of Competitive and Cooperative Systems, American Mathematical Society, 1995. https://doi.org/10.1090/surv/041.

[40] I.M. Sobol', Global Sensitivity Indices for Nonlinear Mathematical Models and Their Monte Carlo Estimates, Math. Comput. Simul. 55 (2001), 271–280. https://doi.org/10.1016/s0378-4754(00)00270-6.

[41] D.S. Stephens, B. Greenwood, P. Brandtzaeg, Epidemic Meningitis, Meningococcaemia, and Neisseria meningitidis, Lancet 369 (2007), 2196–2210. https://doi.org/10.1016/s0140-6736(07)61016-2.

[42] J.M. Stuart, P.M. Robinson, K.A.V. Cartwright, N.D. Noah, Effect of Smoking on Meningococcal Carriage, Lancet 334 (1989), 723–725. https://doi.org/10.1016/s0140-6736(89)90781-2.

[43] B. Sultan, K. Labadi, J.-F. Guégan, S. Janicot, S. Hales, Climate Drives the Meningitis Epidemics Onset in West Africa, PLoS Med. 2 (2005), e6. https://doi.org/10.1371/journal.pmed.0020006.

[44] H.R. Thieme, Uniform Persistence and Permanence for Non-Autonomous Semiflows in Population Biology, Math. Biosci. 166 (2000), 173–201. https://doi.org/10.1016/s0025-5564(00)00018-3.

[45] H.R. Thieme, Spectral Bound and Reproduction Number for Infinite-Dimensional Population Structure and Time Heterogeneity, SIAM J. Appl. Math. 70 (2009), 188–211. https://doi.org/10.1137/080732870.

[46] C.L. Trotter, W.J. Edmunds, Modelling Cost Effectiveness of Meningococcal Serogroup C Conjugate Vaccination Campaign in England and Wales, BMJ 324 (2002), 809. https://doi.org/10.1136/bmj.324.7341.809.

[47] W. Wang, X.-Q. Zhao, Basic Reproduction Numbers for Reaction-Diffusion Epidemic Models, SIAM J. Appl. Dyn. Syst. 11 (2012), 1652–1673. https://doi.org/10.1137/120872942.

[48] World Health Organization, Meningitis, WHO, (2018). https://www.who.int/news-room/fact-sheets/detail/meningococcal-meningitis.

[49] S.P. Yazdankhah, D.A. Caugant, Neisseria meningitidis: An Overview of the Carriage State, J. Med. Microbiol. 53 (2004), 821–832. https://doi.org/10.1099/jmm.0.45529-0.

[50] X.-Q. Zhao, Dynamical Systems in Population Biology, Springer International Publishing, 2017. https://doi.org/10.1007/978-3-319-56433-3.

[51] M. Zorom, H.A. Andrianisa, R. Dorville, P. Zongo, A Spatiotemporal Model of Meningococcal Meningitis with Direct and Indirect Transmission, Math. Methods Appl. Sci. 44 (2021), 11828–11843. https://doi.org/10.1002/mma.6500.